

Fold-Cut Structures with Tunable Stiffness for Multimorphing Soft Robots

Ganguk Lee and Ho-Young Kim*

Versatile changes in shape and mechanical properties can take the adaptability and functionality of soft machines to the next level for operating in complex, inaccessible environments. Soft machines designed with origami or kirigami, the ancient paper art of folding or cutting, have been shown to perform remarkably in severe geometric conditions or situations through shape morphing. However, conventional origami- or kirigami-inspired machines rely on a single, monotonous morphing pathway, thereby limiting their achievable functions. Recent designs integrate both origami and kirigami to enable multimorphing; however, they frequently require numerous actuators or inputs, increasing system complexity. Here, a highly deformable “ori-kirigami” robotic structure is presented by operating both folds and cuts on a 2D tessellated sheet, possessing multiple morphing pathways and tunable mechanical properties. The geometry and mechanics of the ori-kirigami structure are analyzed using theoretical modeling and experiments with paper prototypes. Exploiting these merits, a multimodal soft robot capable of steering into confined gaps and manipulating obstacles encountered in its path is designed and demonstrated. This work can be used to design morphing machines that need to adapt to intricate environments, such as the human body and a disaster area.

1. Introduction

Adaptability and multifunctionality are paramount for soft machines operating various tasks in unstructured, human-inaccessible, harsh environments.^[1–5] Among many attempts to develop the design methodology of soft machines with such capability, the ancient paper arts of folding and cutting, so-called origami and kirigami, have been actively studied to


exploit their capability of 3D large deformations from 2D shapes. Based on the design principles of origami and kirigami, static and dynamic morphologies or mechanical properties (e.g., stiffness and Poisson’s ratio) of the mechanical systems can be engineered by geometric patterns only. More specifically, origami-inspired systems control complex, large deformations effectively via crease patterning. For example, Miura-ori tessellation is an array of a flat foldable degree-4 vertex unit cell, as four creases meet at a single vertex, possessing a single degree of freedom mechanism. By folding only a single unit cell, all cells fold simultaneously, facilitating an efficient bi-axial compression of the entire tessellation structure.^[6,7] Kirigami-inspired systems can possess multiple degrees of freedom since internal constraints are eliminated by cuts. In the case of quadrilateral kirigami tessellation, the sheet can not only deploy in-plane but also buckle out-of-plane.^[8]

Thanks to these advantages, origami and kirigami have been harnessed to solve various engineering problems such as a 2D inverse design of 3D shapes,^[9–11] a design of deployable structures,^[12–14] mechanical metamaterials,^[15–17] and shape-shifting medical devices.^[18,19] For robotic applications, deformable bodies or wheels to overcome various terrains or spatial conditions,^[20–28] tunable stiffness structures for robotic manipulators,^[29,30] and end-effectors^[31,32] were previously proposed. These robots use monotonous, repetitive deployable mechanisms (i.e., folding/unfolding, open-and-close kirigami deployment) for simple robotic functions, such as locomotion, gripping, and shape adaptation. Accordingly, expanding the number of morphing pathways within the robot body enables a proportionally broader scope of robotic functions, giving rise to the development of multimodal robots.^[33]

Recently, synergistic approaches incorporating both origami and kirigami on a single sheet, so-called fold-cut structures (ori-kirigami structures), have garnered interest in an attempt to achieve multiple morphing pathways and diversify potential robotic functions. By introducing additional degrees of freedom, the combination of folds and cuts enables these structures to mimic arbitrary 3D surfaces according to lattice kirigami principles,^[34,35] enhance shape programmability,^[36,37] and regulate mechanical properties.^[38,39] Consequently, these design strategies have facilitated the development of highly deformable modular robots and metamaterials.^[40–46] However, such systems typically require numerous actuators or inputs to manipulate

G. Lee, H.-Y. Kim
 Department of Mechanical Engineering
 Seoul National University
 Seoul 08826, Republic of Korea
 E-mail: hyk@snu.ac.kr

H.-Y. Kim
 Institute of Advanced Machines and Design
 Seoul National University
 Seoul 08826, Republic of Korea

 The ORCID identification number(s) for the author(s) of this article can be found under <https://doi.org/10.1002/aisy.202500229>.

© 2025 The Author(s). Advanced Intelligent Systems published by Wiley-VCH GmbH. This is an open access article under the terms of the Creative Commons Attribution License, which permits use, distribution and reproduction in any medium, provided the original work is properly cited.

DOI: 10.1002/aisy.202500229

each crease, cut, or module individually. For instance, in lattice structures, the folding direction of every crease dictates the final overall shape, thus necessitating multiple actuators for practical implementation.^[40,41,44] Although functional materials such as shape memory polymers (SMP) and liquid crystal elastomers can be employed to simplify actuation and enable reaction to external stimuli, the system can typically be actuated only in a preprogrammed, sequential manner.^[37] Some fold-cut structures leverage multistability to achieve multiple configurations, but these configurations often snap back to equilibrium states quickly, making it impossible to maintain their intermediate shapes and limiting the number of achievable deformation states.^[36,47] Additionally, energy barriers between each stable configuration require the use of high-power density actuators, complicating the design of robots at various scales. To develop a soft machine that harnesses the benefits of origami and kirigami, approaches for effectively controlling multimorphing pathways with a minimum number of actuators and maintaining multiple morphing configurations must be addressed.

In this work, we propose a design strategy for a fold-cut-combined tessellation to yield multimorphing structures and harness them into highly morphable and easily controllable soft robots. We make a variation of Miura-ori tessellation by adding cuts between unit cells which exhibit diverse kinematic behaviors and can morph into multiple states owing to the additional degrees of freedom granted by the cuts. In addition, our origami structure can change its mechanical properties with shape morphing, for which we provide a theoretical explanation as well as experimental measurements. Exploiting these structural characteristics, we fabricate a soft robot by adding locomotive and actuating modules and show the robot's unusual advantages in exploring complex, confined gaps and manipulating obstacles encountered in its path.

2. Results

2.1. Geometry of Fold-Cut-Combined Tessellated Structure

We start from a 2-by-2 unit cell array of Miura-ori tessellation as shown in **Figure 1A**, the well-studied origami pattern which exhibits in-plane auxetic behavior during folding and unfolding. Because every unit cell is connected to adjacent ones along the boundaries, folding a single unit cell inevitably leads to the folding of the whole structure. This system of a single degree of freedom thus has a single morphing pathway between folded and deployed states. We now cut the boundaries of the unit cells except for the four outermost vertices, through which unit cells are connected (**Figure 1B**). We model the connecting vertices as zero-energy bending flexible hinges. Since internal constraints are removed by the cuts, the structure has additional degrees of freedom, i.e., relative rotations between the adjacent unit cells occurring independently of folding within each cell. This combination of origami and kirigami allows the structure to morph into multiple configurations, in contrast to the simple folding and unfolding observed in conventional Miura-ori tessellations (see Movie S1, Supporting Information).

To characterize the multimorphing behavior, we define two angles ρ_x and ρ_y , respectively representing the rotating angles

between two neighboring unit cells about the x - and y -axes. Before studying the relationship between the two angles, we analyzed the geometry of the Miura-ori unit cell (**Figure 1C**). First, the unit cell design is determined by three geometrical parameters of the parallelogram: the lengths of the two sides a and b , and the apex angle γ . Since Miura-ori unit cells have a single degree of freedom folding mechanism, every folding geometry can be represented by a single variable of the folding angle θ , the dihedral angle between the parallelogram and the bottom plane.^[7] The width, length, and height of the unit cell are respectively expressed as

$$w = 2b \frac{\cos \theta \tan \gamma}{\sqrt{1 + \cos^2 \theta \tan^2 \gamma}} \quad (1)$$

$$l = 2a \sqrt{1 - \sin^2 \theta \sin^2 \gamma} \quad (2)$$

$$h = a \sin \theta \sin \gamma \quad (3)$$

The dihedral angles between two adjacent facets that meet at the horizontal and vertical creases, denoted θ_1 and θ_2 , respectively, can each be expressed as

$$\theta_1 = 2\cos^{-1}(\sin \theta) \quad (4)$$

$$\theta_2 = 2\cos^{-1}\left(\frac{\sin \theta}{\sqrt{1 + \cos^2 \theta \tan^2 \gamma}}\right) \quad (5)$$

The relationship between θ , γ , and the diagonal angle between two center-aligned creases of the unit cell, denoted ϵ , can be obtained using spherical trigonometry^[48]

$$\cos \epsilon = -(\cos^2 \gamma + \sin^2 \gamma \cos 2\theta) \quad (6)$$

where $\gamma \in (0, \pi/2)$ and $\theta \in (0, \pi/2)$.

Considering the basic kinematics, the relationship between ρ_x and ρ_y in the Miura-ori-kirigami is found by constraining each other as follows (**Figure 1D**). When ρ_y is zero, the structure can have an internal rotation about the x -axis with the rotation angle $\rho_x \in [-\epsilon, \pi]$. Note that the rotation about the x -axis with negative ρ_x is constrained to $-\epsilon < \rho_x < 0$ unlike the rotation of the opposite direction ($0 < \rho_x < \pi$) because the vertically connected two unit cells contact at $\rho_x = -\epsilon$. When $\rho_y \in (0, \pi)$, it represents the structure with rotational deformation about the y -axis, the rotation about the x -axis being inhibited with $\rho_x = 0$. When the unit cells are completely folded about the y -axis ($\rho_y = \pi$), ρ_x can have a nonzero value between $-\epsilon$ and ϵ . Although intra-unit folding and cut-enabled inter-unit rotation occur separately, the range of the rotating angles is affected by the self-contact constraint.

For ease of control and to avoid floppy behavior of the sheet-originated geometry, a closed unit can be constructed by connecting four unit cells in a round as shown in **Figure 1E**. The ring-like unit can have a finite internal area enclosed by four Miura-ori unit cells (top row of **Figure 1E**) unless the cut-enabled rotation angle $\beta = 0$ or π , giving rise to the overlap of the unit cells as shown in the bottom row of **Figure 1E**. When the unit with a finite internal area ($0 < \beta < \pi$) folds, both the width of the internal area w and the unit cell length l shrink. This auxetic behavior can be quantified by the following Poisson's ratio ν , which is always negative

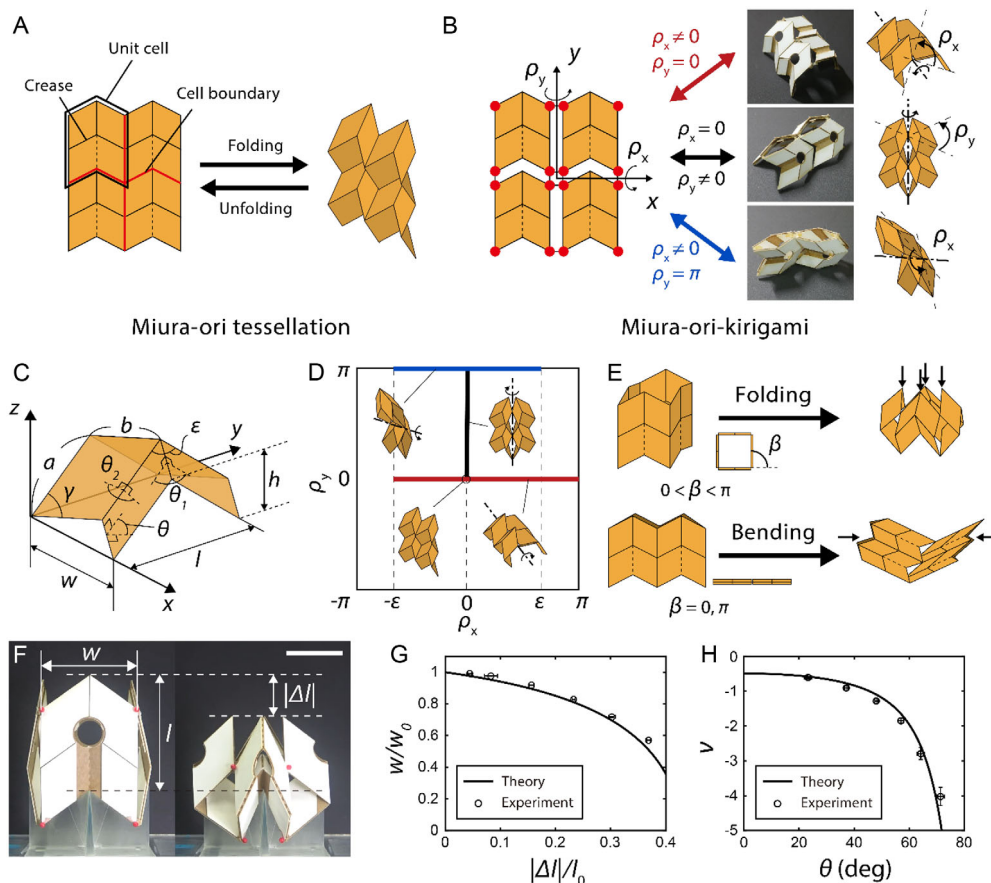


Figure 1. Combination of Miura-ori and kirigami. A) Unimodal morphing of conventional Miura-ori tessellation. B) Multimorphing of Miura-ori-kirigami. ρ_x and ρ_y are the kirigami-enabled rotation angles about x - and y -axis, respectively. The red dots designate the vertices where unit cells are connected. C) Folding geometry of the Miura-ori unit cell. Every projected length indicated is a function of folding angle θ . D) Relationship between two kirigami-enabled rotation angles ρ_x and ρ_y . Each solid line represents the parameter range physically possible for the morphing pathways with the corresponding colors shown in (B). E) Shape-morphing of the Miura-ori-kirigami ring unit. β is a rotation angle between two adjacent unit cells in the ring unit. F) Folding test of the Miura-ori-kirigami ring unit. Folding displacement is the same as the change in unit cell length, Δl . Scale bar, 30 mm. G) Plot of the normalized width versus the normalized displacement of the ring unit during folding. H) Plot of Poisson's ratio versus folding angle θ for the ring unit. In (G,H), solid lines correspond to the theoretical model. Each data point is the average of four measurements. Error bars indicate the standard deviation.

$$\nu = -\frac{l}{w} \frac{dw}{dl} = -\frac{1}{\cos^2 \theta \tan^2 \gamma} \quad (7)$$

We fabricated a prototype of the Miura-ori-kirigami ring unit structure with facets of cardboard and flexible creases (see Figure S1, Supporting Information, for details about design parameters of prototypes) and experimentally verified the foregoing kinematic model through the folding test as shown in Figure 1F. As the ring unit folds, the width w and length l indeed decrease together, exhibiting the auxetic behavior. Figure 1G shows the experimental and theoretical relationship between the width and compression normalized by the initial values of width (w_0) and length (l_0). Since the kinematic models of the Miura-ori unit cell geometry neglect paper thickness, measurement errors are present in the width and length data due to the finite thickness of the paper prototype and the positioning of the red markers. The data were parameterized by the folding angle θ , following the relationships represented in Equation (1) and (2). Using the data in Figure 1G, we numerically calculated Poisson's

ratio, which showed good agreement with the theoretical model in Equation (7) (Figure 1H).

2.2. Tunable Properties via Mode Shifting

One of the major advantages of the tessellation-based structure is its easy expansion by increasing the number of unit cells in either row or column direction. Here, we develop the structure into an m -by- n unit cell array where m and n respectively represent the number of unit cells arranged in the x - and y -directions ($m = n = 4$ in this work), and then connect the vertices on the opposite free-ends in a round to obtain a cylindrical array of Miura-ori-kirigami as shown in Figure 2A. The structure is equivalent to an assembly of four ring units along the y -axis, and it can be deployed by changing the angle β shown in Figure 1E. Two different modes were found when the deployed structure was axially compressed. When $\beta \in (0, \pi)$ (β was set to be $\pi/2$ for stiff mode in Figure 2A), the cylinder exhibits finite folding with nonzero elastic resistance under axial compression. This mode is referred to as

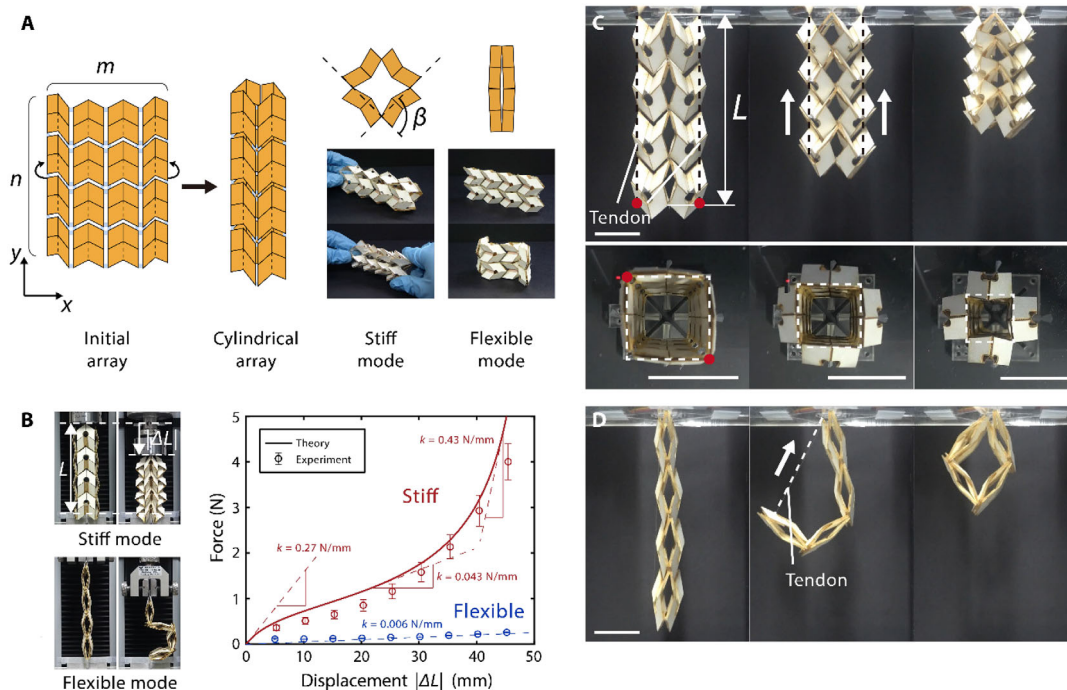


Figure 2. Characterizations of the tunable properties of the Miura-ori-kirigami cylinder. A) Fabrication of Miura-ori-kirigami cylinder and morphologies of stiff and flexible modes. B) Comparison of the compression behaviors of the two modes and force-displacement curves of the stiff (red) and the flexible (blue) modes. Each data point is the average of five measurements and the error bar is the standard deviation. C) Sequential images of contraction of the Miura-ori-kirigami cylinder in the stiff mode (top: side view, bottom: cross-sectional view). Note that the cross-sectional area of the Miura-ori-kirigami cylinder (squares with white dotted lines) shrinks during folding. D) Sequential images of bending of the Miura-ori-kirigami cylinder in the flexible mode. For the shape morphing test in (C,D), two tendons are connected to the bottommost hinges (red dots in (C)) and pulled by servo motors. Scale bars, 30 mm.

the stiff mode. When $\beta = 0$ or π (flexible mode in Figure 2A), it deploys completely flat, and every unit cell meets at a single plane. Thus, the whole structure buckles and bends rather than resisting axial compression, as the hinges axially connecting the unit cells bend. This corresponds to the flexible mode. We can tune the structure's stiffness easily via shape shifting, ranging from the stiff mode to the flexible mode, showing stark contrast in resistance to axial compression (see Movie S1, Supporting Information).

To characterize this tunable behavior, we conducted a compression test for each mode. As shown in Figure 2B, the Miura-ori-kirigami cylinder can carry the load by partially folding its body without bending when in the stiff mode (top row) but collapses and bends freely in the flexible mode (bottom row). To find a reaction force analytically, we assume that every crease in the unit cell is a torsional spring with the length l_c and the spring constant per unit length k_c . As the structure folds, the elastic energy is stored in every crease and the total elastic energy U can be written as

$$U = mnk_cl_c[(\theta_1 - \theta_{1,0})^2 + (\theta_2 - \theta_{2,0})^2] \quad (8)$$

The total potential energy E is a sum of U and the work done by the axial compression force F_c

$$E = U - \int F_c \frac{dL}{d\theta} d\theta \quad (9)$$

where L is the body length, $L = nl$. The principle of minimum potential energy, $dE/d\theta = 0$, allows us to find F_c as

$$F_c = \frac{dU/d\theta}{dL/d\theta} \quad (10)$$

The force-displacement plot in Figure 2B reveals the drastic difference in compression stiffness between the two modes. Our experimental data are consistent with our theory that adopts the empirical crease spring constant per unit length k_c . In the stiff mode, the compression stiffness (the slope of the curve) k changes due to nonlinear folding geometry, which is well-captured by our theory (see Supporting Information for details about compression force modeling). Errors in experimental results arise from hysteresis in the crease layer made of paper due to scars during cyclic folding (loading) and unfolding (unloading). In the flexible mode, the structure shows negligible stiffness compared to the stiff mode.

Such contrast in stiffness results in distinct morphing behaviors of the two modes, as demonstrated in Figure 2C,D. We connected two parallel tendons to the bottommost hinges (red dots in Figure 2C) of the Miura-ori-kirigami cylinder and pulled them in the axial direction using servo motors to deform the cylinder. In the stiff mode, the cylinder is axially compressed while narrowing the cross-sectional area (negative Poisson's ratio) with tendon pulling (Figure 2C). Unable to resist the axial compression, the cylinder in the flexible mode bends with tendon pulling,

eventually forming a circle enclosed by overlapped unit cells (Figure 2D).

2.3. Design, Fabrication, and Characterization of Multimodal Soft Robot

Having introduced the tunable morphology and mechanical properties of the Miura-ori-kirigami structures, we investigate its application as a soft robot. To leverage the structure into robotic systems, we need to consider how to move, morph, and functionalize the structure. We developed a soft robot by assembling modules for mobility and shape morphing as shown in the upper panel of Figure 3A. We used a two-wheeled mobile robot platform (Sony TPH-1000C) as a mobile submodule, which can perform 2D translation and rotation via short-range wireless connection.^[49] We placed two mobile submodules at the front and back so the robot can move back and forth. In the flexible mode, it can also bend the body by reducing the front–rear distance.

We mounted a servo motor on each mobile submodules to pull or release tendons: the front motor for body contraction in the stiff mode and the rear one for flexible–stiff–flat mode switch. The front module controls tendon I which is tied to rear-most hinge of the ori-kirigami structure designated by a blue circle in Figure 3A to apply an axial compression and fold the body. The rear module shifts the robot's mode by applying vertical force to the body for height control using tendons II and III, which are tied to two topmost hinges designated by red circles. For reversible mode shifting, we attached elastic bands at connecting hinges of the body as shown in the lower panel of Figure 3A. The elastic bands stretch as the rear servo motor winds tendons II and III, and recover with the servo unwinding so that the body returns to the initial shape (see Figure S3,

Supporting Information, for details). Every tendon is guided by tendon holes to prevent unwanted tangling.

Figure 3B shows the sequential morphing of the robot using the rear module. The robot mode is determined by how much the tendons are wound. As the mode shifts, the width and height of the robot change simultaneously. In the flexible mode (the left panel of Figure 3B), the body is tall, narrow, and thus easily bendable. By pulling the tendon using the rear module, the body decreases in height and increases in width, consequently opening the inner gap and shifting to the stiff mode (the middle panel of Figure 3B). When the tendons are fully wound, the inner gap closes again and the body shifts to the flat mode (the right panel of Figure 3B). Figure 3C quantitatively shows the coupled relationship between the robot height (H) and width (W). Starting from the upper left point which represents the flexible mode with a minimum width of 90.0 mm and maximum height of 217.9 mm, the robot sequentially morphs into the stiff mode and finally reaches the flat mode with a maximum width of 134.6 mm and minimum height of 115.0 mm. Note that the robot can lower the height up to 53% of its maximum height H_{\max} and can narrow the width up to 67% of the maximum width W_{\max} . At the early stage of the stiff mode, the width remains constant at its minimum value of $W_{\min}/W_{\max} = 0.67$, which corresponds to the width of the mobile submodule rather than that of the Miura-ori-kirigami structure.

We now describe quantitatively the robot functions in each mode, especially the bending (flexible mode) and contraction (stiff mode). In the flexible mode, the robot can rapidly change its body curvature as shown in Figure 3D, with the maximum normalized curvature $|\kappa_{\max}|/L_0 = 4.61$ as displayed in Figure 3E. In the stiff mode, the robot can grip the object owing to the auxetic deformation of the body. To quantify the gripping performance, we theoretically modeled the gripping efficiency η , which represents the

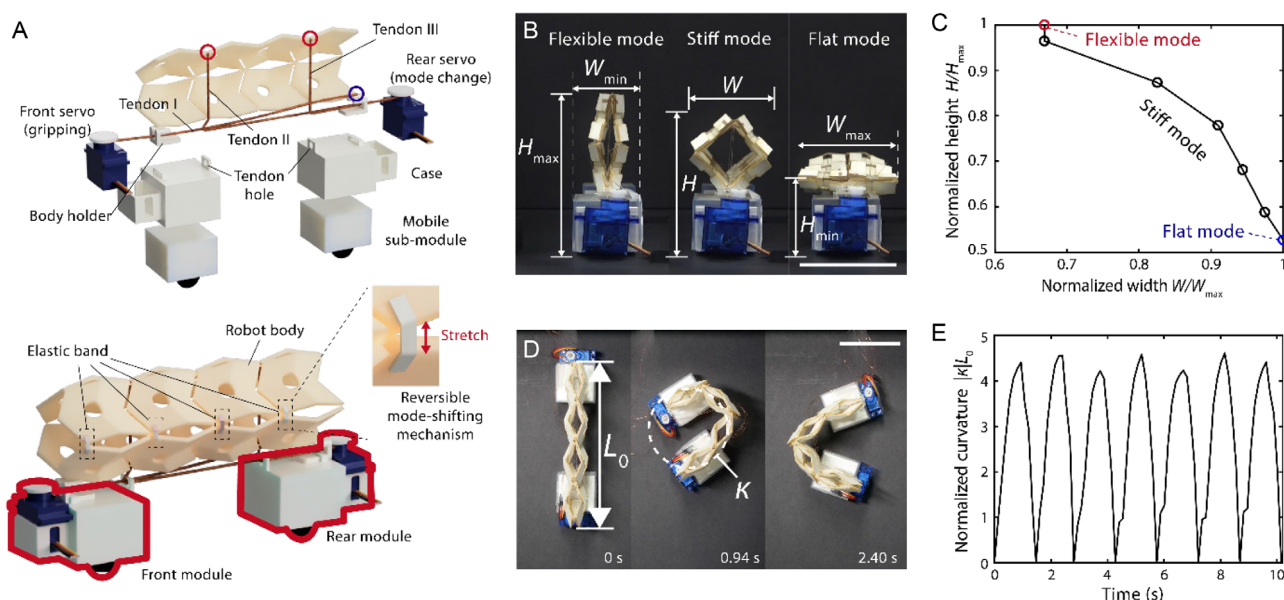


Figure 3. Multimodal soft robot design and characterization. A) Schematic of the soft robot design. Each for exploded view (top) and assembled view (down). B) In situ mode change of the robot from the flexible, stiff, to flat mode. C) Plot of normalized robot height versus normalized width. Red, black, and blue circles indicate the robot shape in flexible, stiff, and flat modes, respectively. D) Rapid change of the body curvature in the flexible mode. For the curvature measurement, five connecting hinges are selected for circle fitting. E) Plot of normalized curvature versus time. Scale bars, 50 mm.

force transmission ratio from the compression force acting on the robot body to the pulling force required to release the object from the robot body, using the principle of minimum potential energy. To verify this model, we experimentally measured the gripping efficiency by pulling a cuboid-shaped object of side length D with a universal testing machine while axially compressing the Miura-ori-kirigami ring unit to grip the cuboid. It is found that η reaches ≈ 0.6 when $D = 0.82w_0$ (see Figure S2, Supporting Information, for details).

2.4. Demonstrations of Robotic Functions

We now demonstrate various functions of our robot possessing shape adaptability and stiffness tunability in situations where

conventional robots have difficulties, as listed in Figure 4A. Because the width and height are easily controlled via in situ mode shifting, the robot can explore through highly narrow or low passages. The robot can also pass narrow curved paths in flexible mode. The auxetic deformation of the body in stiff mode can cause shrinkage of the inner area, which can be exploited for object gripping and manipulation.

Figure 4B shows sequential images of the robot that passes a highly curved narrow path with a gap width of 45 mm (1.3 times larger than the robot's minimum width) and a maximum curvature at the corner of 0.044 mm^{-1} (see Movie S2, Supporting Information). The robot steered into the narrow, curved path in flexible mode by adapting to the surroundings through rapid body curvature change. Figure 4C shows the robot that passes through a

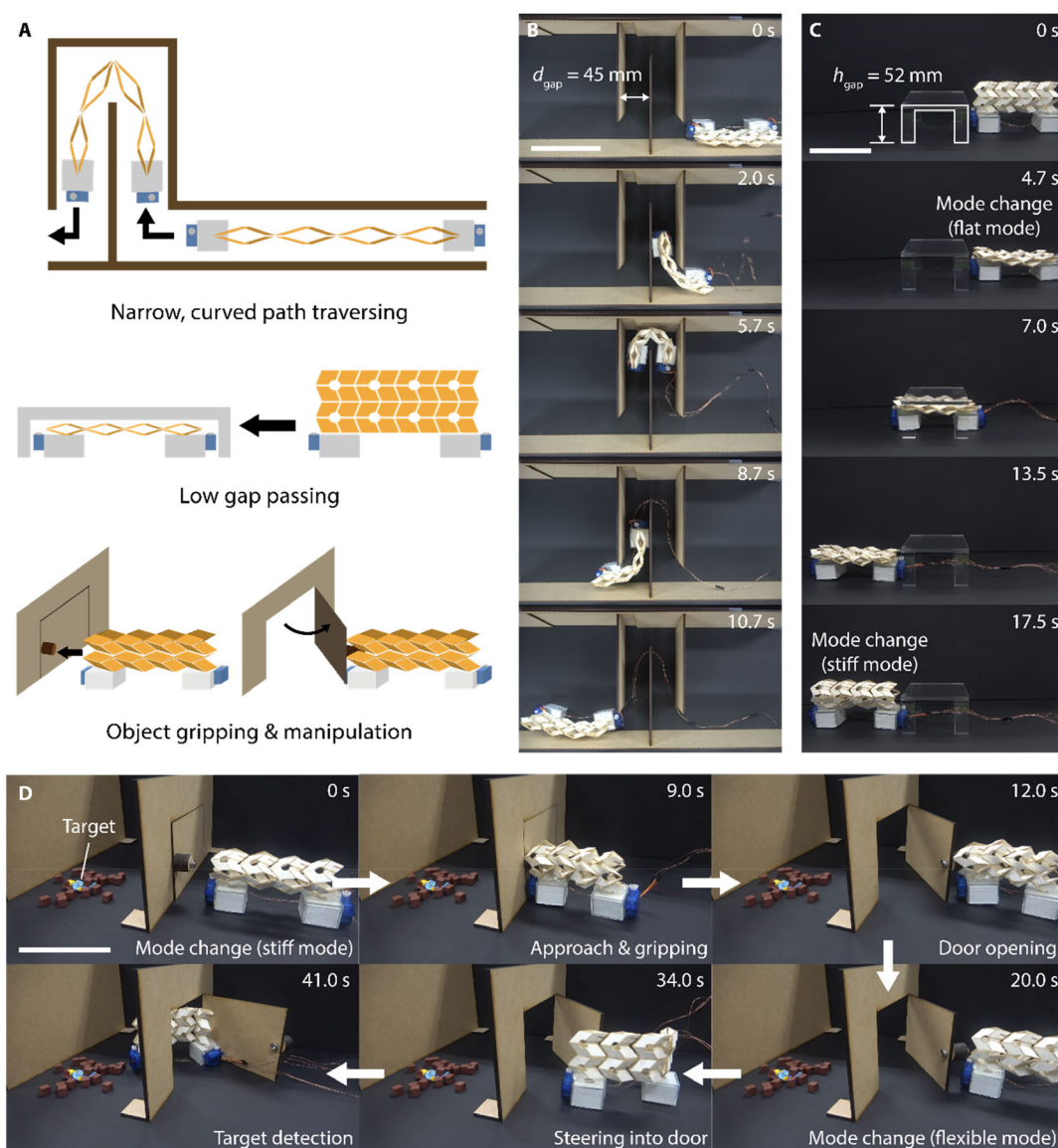


Figure 4. Demonstrations of multiple soft robotic tasks. A) Schematics of multiple robotic tasks. B) Sequential images of narrow, curved path traversing (gap width 45 mm). C) Sequential images of low gap passing (gap height 45 mm). D) Sequential images of opening and passing through a door (gap width 45 mm). Scale bars, 100 mm.

low gap of 52 mm in height (1.2 times the robot's minimum height) by changing the mode from the flexible to the flat (see Movie S3, Supporting Information). Thanks to the elastic bands for reversible deployment, the robot can rapidly recover its initial height after passing the gap. These demonstrated functions that adapt to and navigate through the uneasy passages originate from the kirigami-enabled deployment.

The auxetic properties of body folding in the stiff mode lead to shrinkage of the cross-sectional area of the inner space upon folding, which we now exploit for robotic grasping motion. After our robot grasps the obstacle, the robot can displace it using the mobile submodules. Figure 4D shows the robot entering a closed room by opening the door (see Movie S4, Supporting Information). First, to hold the door handle, the robot shifts into the stiff mode and opens its inner space. The robot grasps the door handle using the shrinkage of the inner area by folding its body with the front actuating module and opens the door by moving back. When the front actuating module unwinds, the body recovers the unfolded shape with the elastic recovery force of the creases, and then the robot releases the door handle. The rear module unwound, the mode shifts back to the flexible mode using the recovery force of the elastic bands, so the robot passes through the opened door and reaches the target.

3. Conclusion

In this study, we have proposed a novel approach to the design of soft actuators, leveraging the benefits of both origami and kirigami. The Miura-ori-kirigami tessellations have highly diversified morphing pathways, compared to the basic origami structures, which consist of folding and cutting-enabled rotations. We revisited the folding geometry of the unit cell, which affects the range of the kirigami deformations, and then, we analyzed the multiple configurations enabled by the cuts kinematically. Auxetic behavior during folding is observed in the 1-by-4 ring unit structure similar to conventional Miura-ori, and the analytical result of Poisson's ratio was consistent with the experimental data.

Expanding the structure by increasing the number of unit cells in an array, we fabricated an ori-kirigami structure that can be deployed from flat to cylindrical shape. We showed analytically and experimentally that the mechanical stiffness varies with its cut-enabled morphing. We exploited our structure into a multimodal soft robot by adding mobile and actuating submodules so it can shift into multiple shapes in situ. The robot exhibits three modes: flexible, stiff, and flat modes, which can be adapted for different functions. In the flexible mode, rapid change in the body curvature is possible without body length change, whereas in the stiff mode, body length can shrink through folding without body curvature change.

Tuning mechanical properties via shape morphing provides a significant advantage for robots working in unstructured sites for exploration, mapping, or rescue. Leveraging the multimorphing and tunable properties of the Miura-ori-kirigami structure, our robot possesses strong capabilities in exploring confined spaces and manipulating objects via adaptive shape-morphing. We demonstrated robot functions in various situations: narrow, curved, low gaps, and blocked areas with obstacles. Although the robot is tethered to the computer by flexible wires for motor actuation

and control, untethered operation is possible using miniature batteries and wireless control.

Owing to the scalable nature of origami and kirigami, our robot design strategy can be employed in diverse engineering applications in complex circumstances and at various scales. However, the selection of actuators for diverse structure sizes remains challenging, especially for microscale robots. By adopting responsive materials for the crease layer (e.g., SMP, dielectric elastomer actuators, and magnetic polymers), machines with enhanced form factors and actuation mechanisms such as lightweight and thin microrobots may be achieved. We expect the fold-cut-combined tessellation structure to be the novel solution for robot design in unstructured conditions ranging from in vivo biomedical applications to disaster areas.

4. Experimental Section

Fabrication of Miura-Ori-Kirigami Paper Prototypes: We fabricated Miura-ori-kirigami prototypes by stacking multiple layers (facet layer on top and bottom, crease layer in the middle) to make a stiffness difference between facets and creases, which justifies the rigid-folding assumption. Cardboard (0.6 mm thick) and kraft paper (0.3 mm thick) were used for the facet and the crease layer, respectively. For the adhesion of the facet and crease layer, double-sided adhesive tape (3M 93015LE) was used. To cut the composite, we used a laser cutter (VLS 3.60DT, Universal Laser Systems). The fabrication process is as follows: 1) Cut the crease lines on two paperboard layers, each for top and bottom facets, respectively. Double-sided tape is attached to one side of each paperboard layer to attach to the crease layer. 2) Attach the kraft paper to one facet layer and perforate the kraft paper along the crease lines. 3) Attach the other facet layer and cut out along the boundary lines. 4) Attach a polyurethane film (PU, 0.4 mm thick) as a connecting hinge material to each unit cell at the connecting vertices using adhesive. 5) Glue the vertices at the opposite free ends together in a round to form a cylindrical structure.

Miura-Ori-Kirigami Ring Unit Folding Test: Four tendons were attached to the four uppermost connecting hinges between unit cells of the ring unit and connected to a 360° continuous servo motor (SG90-HV, TowerPro). The X-shaped fixture was 3D-printed (Form 3, Formlabs) to hold the unit and guide folding during the test. Arduino Uno board was used to control the motor winding. Red markers (3 mm in diameter) were attached with glue at the four outermost vertices to measure the width and length, and the folding sequence was recorded using a digital camcorder (Sony FDR-AX43) at a frame rate of 60 Hz. The width and length of the Miura-ori-kirigami ring unit were collected at 10-frame intervals, and Poisson's ratio was calculated from the width and length experimental data numerically (see Figure S4, Supporting Information, for a detailed schematic of the experimental setup).

Miura-Ori-Kirigami Cylinder Contraction and Bending Test: Miura-ori-kirigami cylinder was hung on x-shaped guide wires attached to an acrylic plate. Two tendons were tied to the two bottommost connecting hinges of the Miura-ori-kirigami cylinder and connected to the servo motors. For the compression test, we used a universal testing machine (34SC-1, Instron) to measure the force and the displacement. The cylinder was compressed with a strain rate of 0.005 s^{-1} for quasi-static approximation. To avoid the self-collapse of the flexible mode cylinder, we attached the cylinder to the upper compression adaptor with adhesive tape. The x-shaped fixture was used to guide the folding and to minimize friction between the paper prototype and the testing bed during the compression. Each test was recorded with the same settings as the ring unit folding test using a digital camcorder (see Figure S5, Supporting Information, for details).

Multimodal Robot Design: We used a tabletop-sized mobile robot (Sony Toio) as a mobile submodule. Two mobile submodules were controlled wirelessly using a desktop computer via Bluetooth connection. Two continuous servo motors (SG90-HV, TowerPro) were controlled with Arduino Uno. Mobile module cases and body holders were fabricated using a 3D

printer (Form 3, Formlabs). To reversibly change the robot modes, elastic bands were fabricated with silicone elastomer (Smooth-sil 950, Smooth-On Inc.) $15 \times 3 \times 0.5$ mm in size (Figure S3, Supporting Information) and were attached to the exterior, near the connecting hinge of the Miura-origami cylinder, using silicone adhesive (SilPoxy, Smooth-on Inc.).

Gripping Test: Cuboid-shaped gripping objects were 3D-printed with side lengths (D) of four sizes ($D = 18, 20, 22, 24$ mm) and a constant height of 40 mm. The servo motor-tendon submodule was connected to the uppermost hinges of the ring unit to grip the object by folding the unit. Compression force was measured using a load cell, and pulling force was measured using the universal testing machine by mounting the object to the machine (see Figure S2, Supporting Information, for details).

Supporting Information

Supporting Information is available from the Wiley Online Library or from the author.

Acknowledgements

The authors are grateful to Prof. Jeong-Yun Sun for helpful discussion. This work was supported by the National Research Foundation of Korea (grant nos. 2018-052541 and 2021-017476) via SNU SOFT Foundry Institute. Administrative support from the SNU Institute of Engineering Research is acknowledged.

Conflict of Interest

H.-Y.K. and G.L. are the inventors on the patent applications (10-2023-0186331, Republic of Korea) submitted by SNU R&DB Foundation that covers the design of fold-cut-combined structure-based multimodal soft robot.

Author Contributions

Ganguk Lee: conceptualization (lead); data curation (lead); formal analysis (lead); investigation (lead); methodology (lead); validation (lead); writing—original draft (lead); writing—review and editing (lead). **Ho-Young Kim:** conceptualization (lead); funding acquisition (lead); project administration (lead); resources (lead); supervision (lead); writing—original draft (lead); writing—review and editing (lead).

Data Availability Statement

The data that support the findings of this study are available in the supplementary material of this article.

Keywords

multimorphing structures, ori-kirigami, soft robots, tunable structures

Received: February 26, 2025

Revised: May 25, 2025

Published online: July 15, 2025

- [1] R. F. Shepherd, F. Ilievski, W. Choi, S. A. Morin, A. A. Stokes, A. D. Mazzeo, X. Chen, M. Wang, G. M. Whitesides, *Proc. Natl. Acad. Sci.* **2011**, *108*, 20400.

- [2] R. K. Katzschmann, J. DelPreto, R. MacCurdy, D. Rus, *Sci. Robot.* **2018**, *3*, eaar3449.
- [3] E. W. Hawkes, L. H. Blumenschein, J. D. Greer, A. M. Okamura, *Sci. Robot.* **2017**, *2*, eaan3028.
- [4] D. Rus, M. T. Tolley, *Nature* **2015**, *521*, 467.
- [5] D. S. Shah, J. P. Powers, L. G. Tilton, S. Kriegman, J. Bongard, R. Kramer-Bottiglio, *Nat. Mach. Intell.* **2021**, *3*, 51.
- [6] K. Miura, *Inst. Space Astronaut. Sci. Rep.* **1985**, *618*, 1.
- [7] M. Schenk, S. D. Guest, *Proc. Natl. Acad. Sci.* **2013**, *110*, 3276.
- [8] A. Rafsanjani, K. Bertoldi, *Phys. Rev. Lett.* **2017**, *118*, 084301.
- [9] L. H. Dudte, E. Vouga, T. Tachi, L. Mahadevan, *Nat. Mater.* **2016**, *15*, 583.
- [10] G. P. Choi, L. H. Dudte, L. Mahadevan, *Nat. Mater.* **2019**, *18*, 999.
- [11] L. Jin, A. E. Forte, B. Deng, A. Rafsanjani, K. Bertoldi, *Adv. Mater.* **2020**, *32*, 2001863.
- [12] E. T. Filipov, T. Tachi, G. H. Paulino, *Proc. Natl. Acad. Sci.* **2015**, *112*, 12321.
- [13] D. Melancon, B. Gorissen, C. J. García-Mora, C. Hoberman, K. Bertoldi, *Nature* **2021**, *592*, 545.
- [14] S. A. Zirbel, R. J. Lang, M. W. Thomson, D. A. Sigel, P. E. Walkemeyer, B. P. Trease, S. P. Magleby, L. L. Howell, *J. Mech. Des.* **2013**, *135*, 111005.
- [15] J. L. Silverberg, A. A. Evans, L. McLeod, R. C. Hayward, T. Hull, C. D. Santangelo, I. Cohen, *Science* **2014**, *345*, 647.
- [16] H. Yasuda, J. Yang, *Phys. Rev. Lett.* **2015**, *114*, 185502.
- [17] Y. Yang, M. A. Dias, D. P. Holmes, *Phys. Rev. Mater.* **2018**, *2*, 110601.
- [18] S. Babaei, Y. Shi, S. Abbasalizadeh, S. Tamang, K. Hess, J. E. Collins, K. Ishida, A. Lopes, M. Williams, M. Albaghdadi, A. M. Hayward, G. Traverso, *Nat. Mater.* **2021**, *20*, 1085.
- [19] H. Suzuki, R. J. Wood, *Nat. Mach. Intell.* **2020**, *2*, 437.
- [20] D. Y. Lee, S. R. Kim, J. S. Kim, J. J. Park, K. J. Cho, *Soft Robot.* **2017**, *4*, 163.
- [21] J. T. Karras, C. L. Fuller, K. C. Carpenter, A. Buscicchio, D. McKeeby, C. J. Norman, C. E. Parcheta, I. Davydchev, R. S. Fearing, *IEEE Inter. Conf. Robotics and Automation (ICRA)*, IEEE, Piscataway, NJ **2017**, pp. 5459–5466.
- [22] M. Luo, R. Yan, Z. Wan, Y. Qin, J. Santoso, E. H. Skorina, C. D. Onal, *IEEE Robot. Autom. Lett.* **2018**, *3*, 1993.
- [23] A. Rafsanjani, Y. Zhang, B. Liu, S. M. Rubinstein, K. Bertoldi, *Sci. Robot.* **2018**, *3*, eaar7555.
- [24] Q. Ze, S. Wu, J. Nishikawa, J. Dai, Y. Sun, C. Zemelka, et al, *Sci. Adv.* **2022**, *8*, eabm7834.
- [25] Y. Yang, Y. Xie, J. Liu, Y. Li, F. Chen, *Soft Robot.* **2024**, *11*, 650.
- [26] B. Seyidoğlu, A. Rafsanjani, *Device* **2024**, *2*, 2.
- [27] Z. Liu, Z. He, H. Xiao, Z. Sun, Q. Ge, J. Xu, H. Fang, *Soft Robot.* **2025**, *12*, 34.
- [28] S. Gao, J. Zhang, R. Zhang, L. Li, J. Cai, Y. Lin, T. Jin, *Soft Robot.* **2025**.
- [29] S. J. Kim, D. Y. Lee, G. P. Jung, K. J. Cho, *Sci. Robot.* **2018**, *3*, eaar2915.
- [30] S. Wu, Q. Ze, J. Dai, N. Udipi, G. H. Paulino, R. Zhao, *Proc. Natl. Acad. Sci.* **2021**, *118*, e2110023118.
- [31] S. Li, J. J. Stampfli, H. J. Xu, E. Malkin, E. V. Diaz, D. Rus, R. J. Wood, in *Inter. Conf. Robotics and Automation (ICRA)*, IEEE, Montreal, QC, Canada **2019**, pp. 7401–7408.
- [32] Y. Yang, K. Vella, D. P. Holmes, *Sci. Robot.* **2021**, *6*, eabd6426.
- [33] C. H. Belke, K. Holdcroft, A. Sigrist, J. Paik, *Nat. Mach. Intell.* **2023**, *5*, 669.
- [34] D. M. Sussman, Y. Cho, T. Castle, X. Gong, E. Jung, S. Yang, R. D. Kamien, *Proc. Natl. Acad. Sci.* **2015**, *112*, 7449.
- [35] C. Dorn, R. J. Lang, S. Pellegrino, *Proc. Royal Soc. A* **2022**, *478*, 20220405.
- [36] X. Zhang, J. Ma, M. Li, Z. You, X. Wang, Y. Luo, K. Ma, Y. Chen, *Proc. Natl. Acad. Sci.* **2022**, *119*, e2117649119.
- [37] Y. Tang, Y. Li, Y. Hong, S. Yang, J. Yin, *Proc. Natl. Acad. Sci.* **2019**, *116*, 26407.

- [38] A. Jamalimehr, M. Mirzajanzadeh, A. Akbarzadeh, D. Pasini, *Nat. Commun.* **2022**, *13*, 1816.
- [39] M. Eidini, G. H. Paulino, *Sci. Adv.* **2015**, *1*, e1500224.
- [40] W. Gao, K. Huo, J. S. Seehra, K. Ramani, R. J. Cipra, in *IEEE/RSJ Inter. Conf. Intelligent Robots and Systems*, IEEE, Piscataway, NJ **2014**, pp. 4598–4604.
- [41] J. T. Overvelde, T. A. de Jong, Y. Shevchenko, S. A. Becerra, G. M. Whitesides, J. C. Weaver, C. Hoberman, K. Bertoldi, *Nat. Commun.* **2016**, *7*, 10929.
- [42] J. T. Overvelde, J. C. Weaver, C. Hoberman, K. Bertoldi, *Nature* **2017**, *541*, 347.
- [43] Y. Li, Q. Zhang, Y. Hong, J. Yin, *Adv. Funct. Mater.* **2021**, *31*, 2105641.
- [44] Y. Li, A. Di Lallo, J. Zhu, Y. Chi, H. Su, J. Yin, *Nat. Commun.* **2024**, *15*, 6247.
- [45] T. Zhao, X. Dang, K. Manos, S. Zang, J. Mandal, M. Chen, G. H. Paulino, *Nature* **2025**, *640*, 931.
- [46] X. Dang, S. Chen, A. E. Acha, L. Wu, D. Pasini, *Sci. Adv.* **2025**, *11*, eads5659.
- [47] N. Nayakanti, S. H. Tawfick, A. J. Hart, *Extreme Mech. Lett.* **2018**, *21*, 17.
- [48] C. D. Santangelo, *Ann. Rev. Condens. Matter Phys.* **2017**, *8*, 165.
- [49] toioTM core cube specifications (Sony Interactive Entertainment Inc, <https://toio.github.io/toio-spec/en/> **2021**).